Article

Investigation of Rotor Efficiency with Varying Rotor Pitch Angle for a Coaxial Drone

Knut Erik Teigen Giljarhus [1,*] , Alessandro Porcarelli [2] and Jørgen Apeland [3]

1   Department of Mechanical and Structural Engineering and Materials Science, University of Stavanger, PB 8600, 4036 Stavanger, Norway
2   Neptech AB, Enskededalen, 121 34 Stockholm, Sweden; alessandro@neptech.se
3   Nordic Unmanned AS, Rådhusgata 3, 4306 Sandnes, Norway; ja@nordicunmanned.com
*   Correspondence: knut.e.giljarhus@uis.no

Abstract: Coaxial rotor systems are appealing for multirotor drones, as they increase thrust without increasing the vehicle's footprint. However, the thrust of a coaxial rotor system is reduced compared to having the rotors in line. It is of interest to increase the efficiency of coaxial systems, both to extend mission time and to enable new mission capabilities. While some parameters of a coaxial system have been explored, such as the rotor-to-rotor distance, the influence of rotor pitch is less understood. This work investigates how adjusting the pitch of the lower rotor relative to that of the upper one impacts the overall efficiency of the system. A methodology based on blade element momentum theory is extended to coaxial rotor systems, and in addition blade-resolved simulations using computational fluid dynamics are performed. A coaxial rotor system for a medium-sized drone with a rotor diameter of 71.12 cm is used for the study. Experiments are performed using a thrust stand to validate the methods. The results show that there exists a peak in total rotor efficiency (thrust-to-power ratio), and that the efficiency can be increased by 2% to 5% by increasing the pitch of the lower rotor. The work contributes to furthering our understanding of coaxial rotor systems, and the results can potentially lead to more efficient drones with increased mission time.

Keywords: computational fluid dynamics; blade element momentum theory; coaxial rotor; aerodynamics

1. Introduction

Several designs for unmanned aerial vehicles exist today, with varying compromises in terms of size, fuel system and speed [1]. Multirotor drones have the advantage of small footprint, non-restrictive take-off/landing area requirements, high maneuverability and high hovering capability. Multirotor drone designs can be found in sizes ranging from light vehicles below 50 g [2,3] to larger vehicles designed for human transport [4,5].

The power unit on a multirotor drone is important, as it determines the type of operations a drone can perform. The most common power source on multirotor drones is batteries, although some designs exist that employ, e.g., hydrogen [6,7]. Increasing the efficiency of the drones is important as it can extend the flight time, thereby extending mission time or even enabling new types of mission capabilities.

The projected area of a drone can be a critical factor, as it determines how the drone can be transported and the type of areas it can fly in. In a coaxial rotor system, one rotor is put above the other instead of placing them side by side. Compared to larger aircrafts, coaxial multirotor drones typically use fixed-pitch rotors to avoid complex mechanical design [8]. The coaxial layout increases the thrust without increasing the projected area, making this an attractive option for multirotor drones.

However, a disadvantage of a coaxial rotor system is that there is a loss of efficiency, since the lower rotors operate in the wake of the upper rotors. Some attempts have

been made to increase the efficiency by adjusting the distance between the rotors [9–11]. There are also some commercial designs using a different pitch for the lower rotor (e.g., CarbonCore Cortex X8 and Himax CR2816), and this has been proposed as a way to increase the efficiency [12]. Although several studies on coaxial rotors exist in the scientific literature, the influence of pitch has not been thoroughly explored. Most studies have also been performed on larger rotors with systems for dynamically changing the collective pitch of the blades, while in recent years, smaller drones with fixed pitches are becoming increasingly relevant.

Yoon et al. [13] investigated changing the collective pitch of the lower rotor in a coaxial system using detailed computational fluid dynamics (CFD) simulations. The study used the XV-15 rotor with a diameter of 3.8 m. The emphasis was on balancing torque by adjusting the pitch and the impact on thrust-to-power efficiency was not investigated. Jinghui et al. [14] performed both wind tunnel tests and CFD simulations of a coaxial rotor system with large blades of 4 m in diameter. This study also found that the thrust on the lower rotor was lower than the upper since the effective angle of attack is lower, but did not investigate the effect on efficiency of modifying the pitch of the lower rotor. Kim et al. [15] used CFD simulations to study the efficiency of a coaxial rotor setup for a conceptual personal air vehicle. They found that the optimal pitch for the upper rotor was different than that of the lower rotor, but they did not perform simulations specifically with different pitches for the two rotors. Leishman and Ananthan [16] looked specifically at the influence of pitch angle in a coaxial rotor system. They performed simulations using blade element momentum theory (BEMT) of a 7.6 m Harrington helicopter rotor in a coaxial configuration. They found an optimal design where the pitch of the lower rotor is higher than the upper rotor for the downwash region, with a slightly lower pitch than the upper rotor for the outer part of the rotor.

This work uses a combination of simplified analysis with blade element momentum theory and detailed blade-resolved CFD simulations to investigate the influence of changing the pitch of the lower rotor in a coaxial system for a medium-sized drone. Experiments in single-rotor and coaxial rotor setups are performed to validate the computational models. The main contributions of the paper are to demonstrate that a simplified BEMT model can give reasonable results for coaxial rotors with varying pitch angles, and also to provide insight into the impact of using different pitch angles for the upper and lower rotor.

2. Computational Methods

2.1. Blade Element Momentum Theory

Blade element momentum theory (BEMT) combines two theories; momentum theory and blade element theory. In momentum theory the rotor acts as a disk injecting momentum into the flow, while in blade element theory, the rotor is divided into small, independent elements and aerodynamic forces are calculated using tabulated values for lift and drag for the airfoil. The methodology has been extensively used for both rotor systems and wind turbines, and detailed derivations can be found elsewhere [17–19]. Hence, only a brief explanation of the method applied in this study is given here. Figure 1 gives an overview of both the momentum theory control volume and the blade element theory approach.
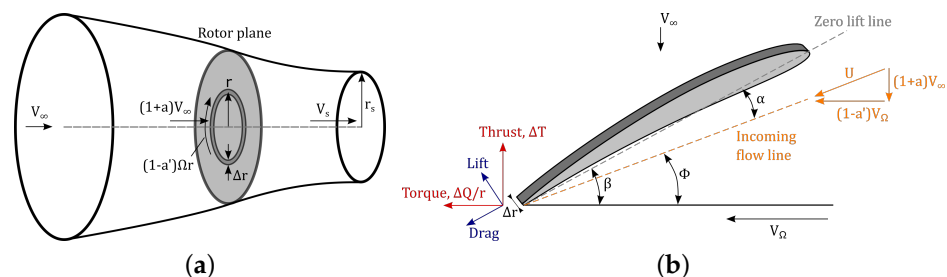

Figure 1. Illustration of parameters and forces for blade element momentum theory. (**a**) Momentum theory control volume. (**b**) Blade element.

For a propeller, power is applied to the rotor to generate thrust along the rotation axis. The incoming velocity that a blade element is subjected to is not a simple addition of the flow velocity in the axial direction and the angular velocity of the rotor in the tangential direction. The axial velocity is accelerated due to the presence of the rotor and the tangential velocity is reduced due to swirl. This can be accounted for by introducing axial and tangential induction factors,

$$v = (1 + a)V_\infty, \tag{1}$$

$$v' = (1 - a')V_\Omega = (1 - a')\Omega r, \tag{2}$$

$$U = \sqrt{v^2 + v'^2}, \tag{3}$$

where v and v' are axial and tangential velocities, and a and a' are the axial and tangential induction factors, respectively. U is the incoming velocity seen from the blade element.

In blade element theory, the force on a single blade element can be expressed by

$$\Delta T = \sigma \pi \rho U^2 C_T r \Delta r, \tag{4}$$

$$\Delta Q = \sigma \pi \rho U^2 C_Q r^2 \Delta r, \tag{5}$$

where T is the thrust, i.e., force in axial direction, and Q is the torque, i.e., the moment around the axial direction. $\sigma = Bc/(2\pi R)$ is the blade solidity, where B is the number of blades and c is the chord length. The thrust and torque coefficients in the above expressions are calculated as

$$C_T = C_L \cos \phi - C_D \sin \phi, \tag{6}$$

$$C_Q = C_L \sin \phi + C_D \cos \phi. \tag{7}$$

The drag and lift coefficients, C_D and C_L, respectively, are extracted from tabulated values for the airfoil using the local angle of attack for the airfoil,

$$\alpha = \beta - \phi. \tag{8}$$

Similar expressions as in Equations (4) and (5) for the incremental forces can also be found from momentum theory,

$$\Delta T = 4\pi \rho r V_\infty^2 (1 + a)a\Delta r, \tag{9}$$

$$\Delta Q = 4\pi \rho r^3 V_\infty \Omega (1 + a)a'\Delta r. \tag{10}$$

Combining these equations, the induction factors can be expressed directly as

$$a = \frac{1}{\kappa - 1}, \tag{11}$$

$$a' = \frac{1}{\kappa' + 1}, \tag{12}$$

$$\kappa = \frac{4 \sin^2 \phi}{\sigma C_T}, \tag{13}$$

$$\kappa' = \frac{4 \sin \phi \cos \phi}{\sigma C_Q}. \tag{14}$$

From the rotor force diagram for a blade element, Figure 1, the local inflow angle ϕ can be expressed from the local velocities as

$$\tan \phi = \frac{(1 + a)\Omega R}{(1 - a')V_\infty}. \tag{15}$$

Once a solution for the inflow angle is found, the forces are calculated from the blade element equations and integrated along the rotor to find the total forces. A well-known

issue with BEMT methods is the overprediction of forces near the tip, since vortex shedding from the tip is not accounted for in the induced velocities. This is typically alleviated by the use of tip-loss correction methods. In this work, the classic Prandtl tip-loss method is used [20], where a correction factor, F, is multiplied into the expressions for thrust and torque for each element, Equations (9) and (10). This expression factor is given as

$$F = \frac{2}{\pi} \cos^{-1} e^{-f},$$ (16)

$$f = \frac{B}{2} \frac{R-r}{r \sin \phi}.$$ (17)

The above method is implemented in the open source software pyBEMT [21], developed by one of the authors. Equation (15) is solved for ϕ using root-finding functions from the `SciPy` library [22].

Note that for the hover situation considered in this work, Equation (15) is not defined since the axial inflow velocity is zero. To circumvent this, this velocity is instead set to a low value, $V_\infty = 1 \times 10^{-6}$.

The modelling of the coaxial rotor is based on momentum theory [17,23]. The lower rotor will be in the slipstream created by the upper rotor. Some authors have been considering the varying slipstream contraction [24], but here a fully developed slipstream will be considered. Additionally, it is assumed that the rotors are hovering, i.e., there is a zero velocity inflow to the upper rotor, and that the lower rotor is a sufficient distance below the upper rotor so that the slipstream is fully developed. For this case, the continuity equation gives

$$V_i \pi R^2 = V_s \pi R_s^2,$$ (18)

where V_i is the induced velocity just below the rotor and V_s is the slipstream velocity in the fully developed wake. R_s is the radius of the slipstream region. For the momentum, the thrust generated from the upper rotor is equal to the change in momentum from the static region to the slipstream,

$$T = \rho V_i A V_s.$$ (19)

Finally, the work done by the upper rotor is equal to the kinetic energy in the slipstream

$$T V_i = \frac{1}{2} \rho V_i A V_s^2.$$ (20)

From these equations, the following expressions for the slipstream properties are found:

$$R_s = \frac{R}{\sqrt{2}}$$ (21)

$$v_s = C_s \sqrt{\frac{2T}{\rho A}}$$ (22)

Here, C_s is a model constant, accounting for the fact that for smaller UAV rotors, the hub is a large part of the rotor, and there is not a sharp transition from the hub of the rotor to the rotor, or from the slipstream to the outer part of the lower rotor. In this work, this constant is set to $C_s = 0.8$. Additionally, the model assumes that the velocity tapers linearly off from the slipstream to the outer part. The end of this taper region is set to the middle of the slipstream radius and the radius of the rotor.

For the pitch adjustment of the lower rotor in the coaxial setup, it is desirable to maintain the same thrust when the pitch is modified. This is achieved by adjusting the angular velocity of the lower rotor to obtain the same total thrust. In the BEMT solver, the root-finding functions of the `SciPy` library are used for this purpose.

2.2. Computational Fluid Dynamics

Several detailed simulation methods for rotor systems based on CFD methodology exist today. These include blade-resolved methods where the blade is explicitly modelled [13,25–28] and methods where the blade is modelled using embedded BEMT methods or similar techniques and then represented as a volume force in the CFD simulation [29–31].

In this work, the blade-resolved method is used. The CFD simulations are performed by solving the transient, incompressible Reynolds-averaged Navier–Stokes equations, together with the k-omega shear stress transport (SST) turbulence model [32]. In Yoon et al. [26], it was found that an eddy-resolved method performed better than the Reynolds-averaged approach for rotor flows. However, this was because the eddy viscosity grows in the far-field due to how the turbulent length scale is modelled in the Spalart–Allmaras (SA) turbulence model. The turbulence length scale in the SA model is dependent on the distance from the wall, thereby growing larger than typical eddy sizes in the far-field. In the k-omega SST model, the turbulence length scale is $l_t \sim \sqrt{k}/\omega$, thereby circumventing this issue.

The simulations are performed using the open source software OpenFOAM [33,34] v7, which is based on the finite volume method. The PIMPLE algorithm is used for the pressure–velocity coupling and the time marching. This algorithm allows a larger time step to be taken while maintaining numerical stability, combining outer pressure-momentum corrections with inner pressure corrections. Here, the rotor is allowed to rotate 1° per time step. Up to 50 outer correctors are used, reducing the sub-iteration residual by three orders of magnitude at each time step. The implicit Euler scheme is used for temporal discretization. For the spatial discretization, second-order schemes are used for all terms, and in particular, the upwind-weighted `linearUpwind` scheme is used for the convective terms.

Rotation of the rotors is handled using Arbitrary Mesh Interface (AMI). A cylindrical domain around the rotor is meshed separately and allowed to rotate at a constant angular velocity. This region is then coupled to the surrounding static mesh using the `cyclicAMI` boundary condition. At each time step, each face at the AMI boundary identifies overlapping faces from the neighboring patch and the contribution from these faces is weighted according to the intersecting area [35].

As for the BEMT solver, when a case is solved with a modified pitch for the coaxial rotor setup, the angular velocity should be modified to maintain the same total thrust. This is achieved by writing a custom version of the solid body motion solver in OpenFOAM, where the angular velocity is adjusted during the simulation using a binary search algorithm until the desired total thrust is found.

The simulations are run in parallel on a cluster using Intel Xeon E5-2695 v4 processors. With the case decomposed over 108 cores, a single simulation of 10 full rotor revolutions has an execution time of approximately 40 h.

3. Numerical Setup

3.1. Rotor Geometry

The main parameters of the rotor geometry are listed in Table 1. The geometry is based on the commercial T-MOTOR G28x9.2 carbon fiber rotor, which has diameter $D = 28'' = 71.12$ cm and pitch $P = 9.2'' = 23.368$ cm. This rotor size is chosen as it is used in several commercial designs [36,37] and in research [11,38], due to giving sufficient thrust for industrial payloads while maintaining a reasonable footprint for transportation and storage.

Table 1. Description of rotor geometry.

Quantity	Unit	Value
Rotor diameter, *D*	cm	71.12
Number of blades	-	2
Hub diameter	cm	5.4
Pitch at 0.75*R*	in	9.2
Chord at 0.75*R*	cm	4.4

The chord length is kept fixed for all blades, based on measurements of the T-MOTOR rotor. The twist angle of the blade is varied according to the following formula,

$$\beta(r) = \arctan\left(\frac{P}{2\pi r}\right),\tag{23}$$

where *P* is the pitch at 0.75*R* given in metres, except close to the hub of the blade where the twist is gradually reduced to yield a geometry suitable for manufacturing. The twist angles considered in this work along with the chord length along the blade span are shown in Figure 2.
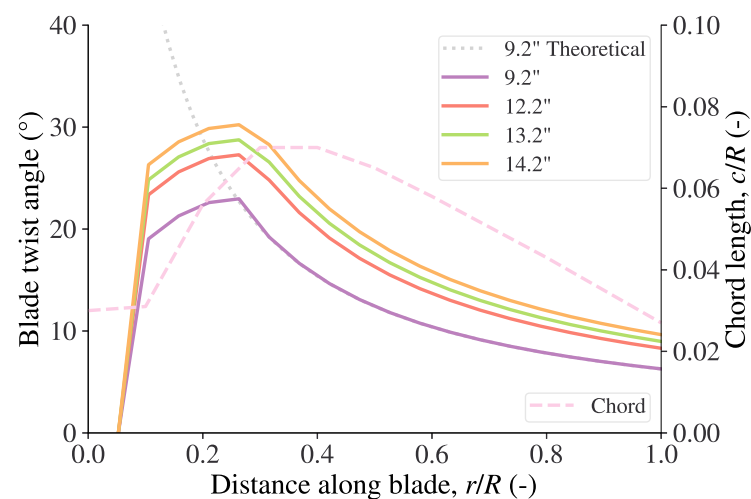
Figure 2. Twist angle and chord length of the rotor blade.

For consistency, the rotor geometry is constructed using a single airfoil instead of using the actual airfoil shape from the commercial rotor. The chosen airfoil is the Archer A18 airfoil, originally built for free-flight airplanes [39]. The coordinates for the airfoil are taken from the UIUC Airfoil Coordinates Database [40]. A comparison of the A18 airfoil against measurements of the commercial rotor is shown in Figure 3. Although there are some discrepancies, especially towards the trailing edge where a thin edge is challenging to manufacture for small rotors, the overall agreement is good. The tip of the rotor is also simplified compared to the commercial airfoil, with a simple cut-off at the tip of the blade. Figure 4 shows the 3D geometry used in the CFD simulations.
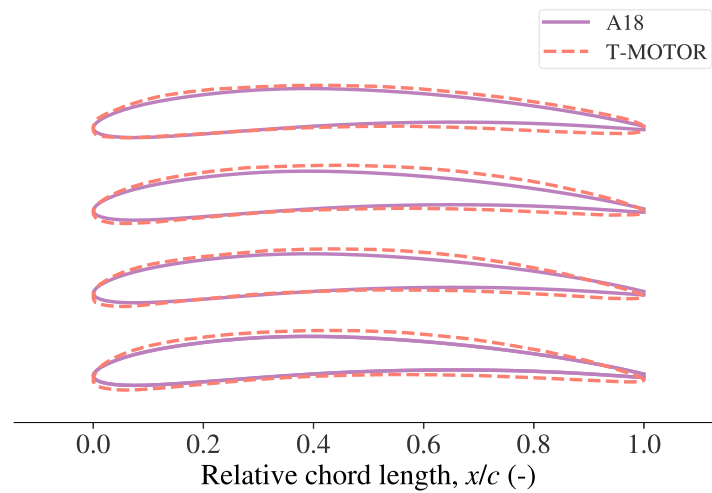
Figure 3. Comparison of A18 airfoil against airfoils along the commercial T-MOTOR G28x9.2″ blade at four radial stations. From the bottom: 0.3*R*, 0.5*R*, 0.7*R*, 0.9*R*.
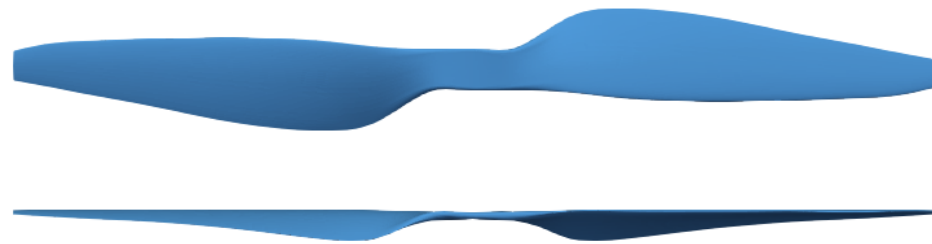

Figure 4. Top view (**top**) and front view (**bottom**) of the computational 3D rotor geometry for a pitch of 9.2″.

The aerodynamic drag and lift coefficients for the airfoil, to be used in the BEMT solver, are obtained by performing XFOIL simulations through the QBlade interface [41,42]. For the sake of simplicity, a constant Reynolds number of Re = 175,000 is used, which is approximately the Reynolds number at $r = 0.75R$ at a rotational speed of 2000 RPM. The resulting drag and lift coefficients, along with the aerodynamic efficiency (drag-to-lift ratio), are shown in Figure 5. The airfoil reaches a peak in aerodynamic efficiency of $C_L/C_D = 80$ at angle of attack $\alpha = 5°$.
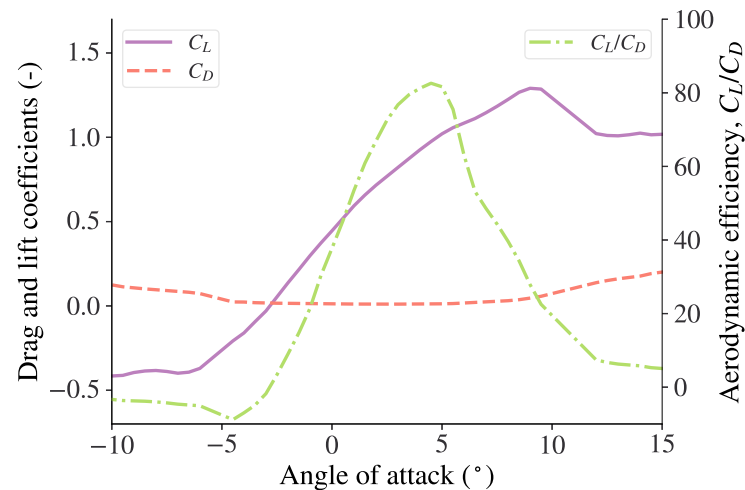

Figure 5. Aerodynamic drag and lift coefficients for the A18 airfoil, calculated using XFOIL at Re = 175,000.

3.2. Mesh

The numerical simulations are performed over a mixed-element unstructured grid developed at neptech AB using Pointwise® (Cadence Design Systems, San Jose, CA, USA) [43], a mesh-generation software specifically developed for CFD applications. Particular attention is paid to the rotor surface mesh, which is shown in Figure 6a. Stretched anisotropic quadrilaterals have been extruded from the leading edge and the trailing edge using the 2D T-Rex algorithm. T-Rex allows us to grow layers of rectangular cells given the first cell thickness and a growth factor, and the inflation is stopped once a smooth dimensional transition with the rest of the surface mesh is achieved. The rest of the upper and lower surface domains consist of triangles and quads generated by the "advancing front ortho" algorithm, and are automatically shaped to comply with high-quality criteria, whilst fulfilling a specified maximum cell dimension. The grid at the blunt trailing edge and at the wingtip has been designed to transition smoothly to the T-Rex-extruded upper and lower surface cells using a structured-dominant approach.

Once a reasonably fine and high-quality 2D grid is obtained, the 3D T-Rex algorithm is employed to inflate layers of high-aspect-ratio hexahedra and prisms in the near-wall region to effectively capture viscous effects. The remaining AMI block is filled with isotropic tetrahedra. As shown in Figure 6b, T-Rex ensures a smooth dimensional transition between the last extruded prism or hexahedron and the outer tetrahedra through one layer of high-quality pyramids. The remainder of the far-field domain surrounding the AMI blocks is cylindrical and fully consists of isotropic tetrahedra with increased characteristic dimension (Figure 6c). In order to achieve a more detailed solution in the far-field for the wake immediately downstream of the rotor, a cylindrical source has been shaped enclosing this region to introduce a local grid refinement.
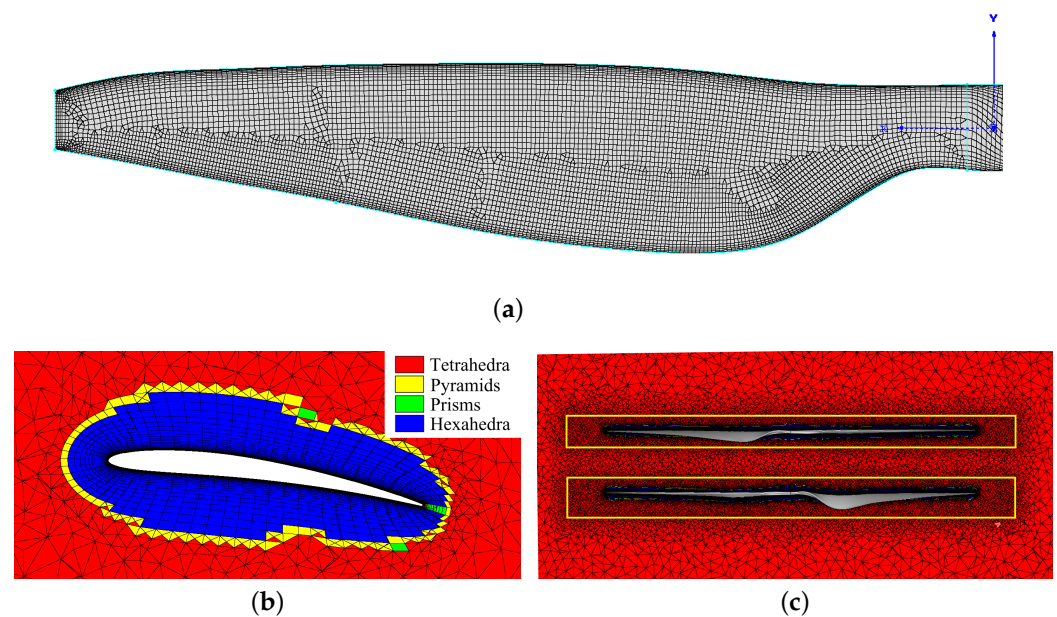

(**a**)

(**b**)　　　　　　　　　　　　　　　　　　　　　(**c**)

Figure 6. Illustration of mesh arrangements. (**a**) Rotor surface mesh. (**b**) Close-up of mesh near rotor with layers generated using 3D T-Rex extrusion. (**c**) Mesh around rotors. The yellow rectangles indicate the AMI blocks.

The geometric dimensions of the cylindrical source and mesh blocks are reported in Table 2. The lower AMI block height has been adjusted to fit with the increased pitch of the lower rotors. The values of the most relevant grid setup parameters are summarised in Table 3.

Pointwise's mesh quality-check tool can effectively cope with the strict constraints of OpenFOAM. For instance, the solver is particularly sensitive to cells showing a high non-orthogonality, which can potentially lead to simulation divergence. A reasonable trade-

off between cost efficiency and cell quality has been found, with the number of severely non-orthogonal cells (>70) reduced to less than 600 per AMI block and grouped in non-critical flow regions. Preliminary simulations provided a reasonably stable solution. Figure 7 shows the y^+ values over the blades at $r = 0.75R$. The y^+ value is lower than one over the majority of the rotor surface, except in a small region at the leading edge. It is overall lower than two across the entire blade, thus indicating a satisfactory resolution for the viscous effects.
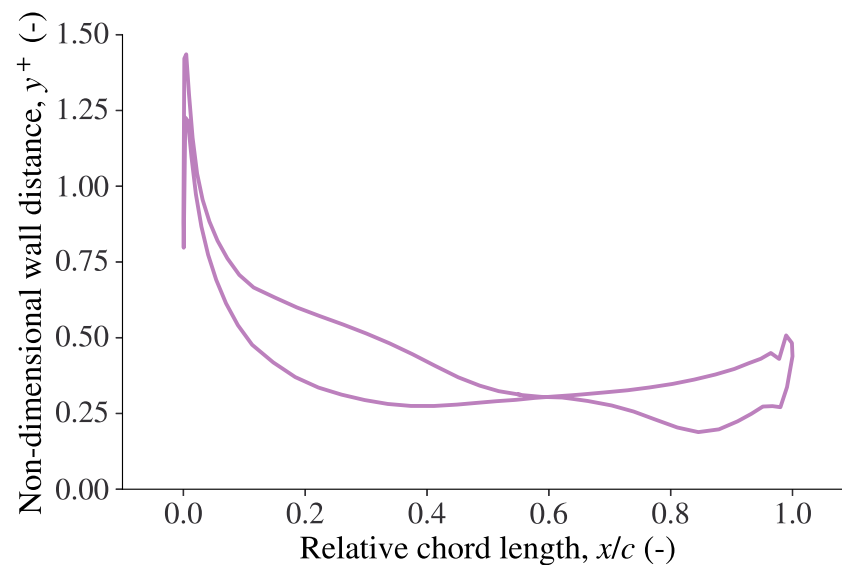

Figure 7. Non-dimensional wall distance along rotor surface at radius $r = 0.7R$ for RPM = 2200.

Table 2. Mesh size parameters for the cylindrical blocks and source.

Object	Base Diameter	Height	Ratio to D
Upper AMI block	84.0 cm	5.50 cm	
Lower AMI block	84.0 cm	6.95 cm	
Cylindrical source	1.00 m	3.00 m	~4 D
Far-field block	10.0 m	10.0 m	~14 D

Table 3. Main mesh setup parameters.

Quantity	Unit	Value	Ratio to D
Rotor surface maximum cell size	mm	2.00	$\sim D/350$
3D T-Rex 1st layer thickness	m	1×10^{-5}	
3D T-Rex inflation growth factor	-	1.2	
AMI block maximum cell size	mm	5.00	$\sim D/140$
Source delimited region max. cell size	cm	2.00	$\sim D/35$
Far-field block maximum cell size	cm	20.0	$\sim D/4$
Total number of cells	-	14.1×10^6	

4. Experimental Setup

The experiments are performed on a RCbenchmark Series 1780 dynamometer and thrust stand. The experimental setup is shown in Figure 8. The rotors used are T-MOTOR G28x9.2 rotors, driven by T-MOTOR U8II KV100 brushless motors with power supplied by 1500 W power supplies. For the coaxial setup, the rotors are mounted facing each other and rotating in opposite directions.

The angular speed is measured by an optical tachometer, and the thrust and torque are measured by a load cell with a given experimental tolerance of $\pm 0.5\%$.
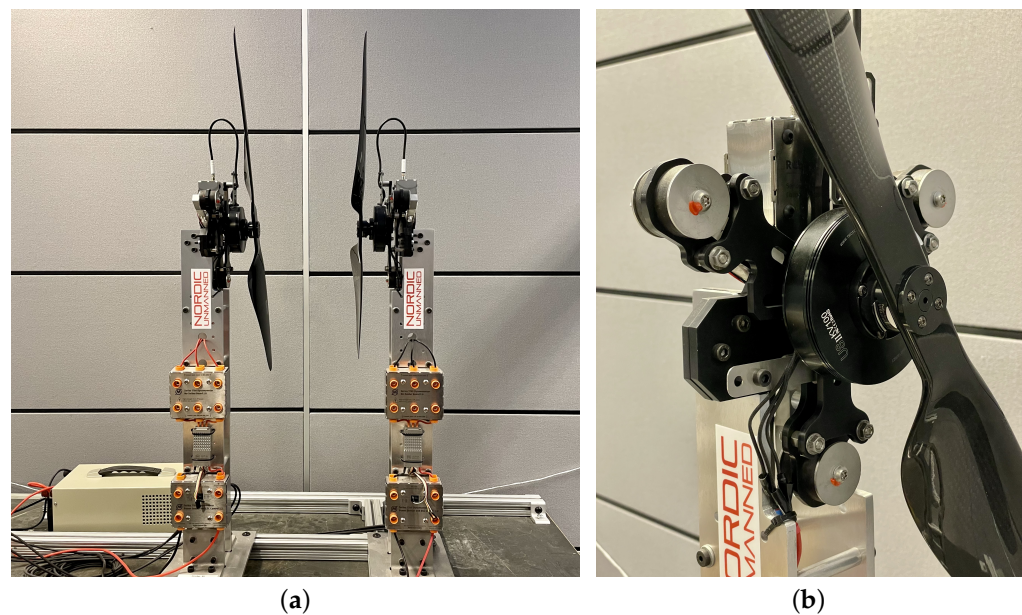
Figure 8. Picture of experimental setup showing the thrust stand in coaxial configuration and a close-up view of the load cell and motor. (**a**) Thrust stand. (**b**) Load cell and motor.

5. Validation

5.1. Mesh Sensitivity Study

The reliability of the mesh was tested through a mesh sensitivity study for a single rotor. When designing a refined and coarser mesh setup, it was found that changes in the cell dimension over the rotor surface grid resulted in poorer quality 3D blocks, with an increased number of severely non-orthogonal cells. This phenomenon can affect the solution stability and thus lead to a non-reliable mesh sensitivity study. Therefore, in order to provide setups with overall similar quality, the characteristic maximum dimension of the tetrahedra of the AMI block was varied. This parameter was increased to 10.0 mm for the coarser setup and decreased to 3.75 mm in the finer setup. Table 4 shows the total number of cells of the three configurations along with their simulation results. The coarse setup solution highlights a reasonable but non-negligible change in thrust and efficiency compared to the chosen medium setup. In contrast, the fine setup shows only minor differences, hence the medium mesh is chosen for the remainder of the simulations in this work.

Table 4. Mesh sensitivity study.

Number of Cells ($\times 10^6$)	Thrust (N)	Efficiency (N W^{-1})
5.50	25.5	0.124
8.78	25.9	0.127
13.2	26.0	0.127

5.2. Single-Rotor Validation

Figure 9a shows a comparison of the computed thrust with BEMT and CFD against the experimental values for varying angular velocities. Included also are data from the vendor for the T-MOTOR G28x9.2 rotor [44]. The vendor data are in good agreement with the performed experiments, acting as validation of the experimental setup. The CFD simulations match the trend of the experiments, but predict thrust values to be approximately 15% lower. It should be noted that since the simulated rotor geometry does not exactly match the commercial rotor design, an exact match can not be expected. In particular, the tip design of the commercial rotor is expected to be more efficient than the simulated

design. The BEMT results are also in good agreement with the experiments, but with increasing underprediction at higher angular velocities.

Figure 9b shows a comparison of the computed efficiency with BEMT and CFD against the experimental values for varying angular velocities. The efficiency is defined as the thrust-to-power ratio, where the power is calculated as the torque multiplied by the rotational velocity. Similar trends as for the thrust are observed here. The CFD simulations are close to the experiments, with an underprediction of approximately 2% to 5%. The BEMT simulations also follow the same trend as the experiments but with an overprediction ranging from around 15% at low rotational speeds to 5% at high rotational speeds.
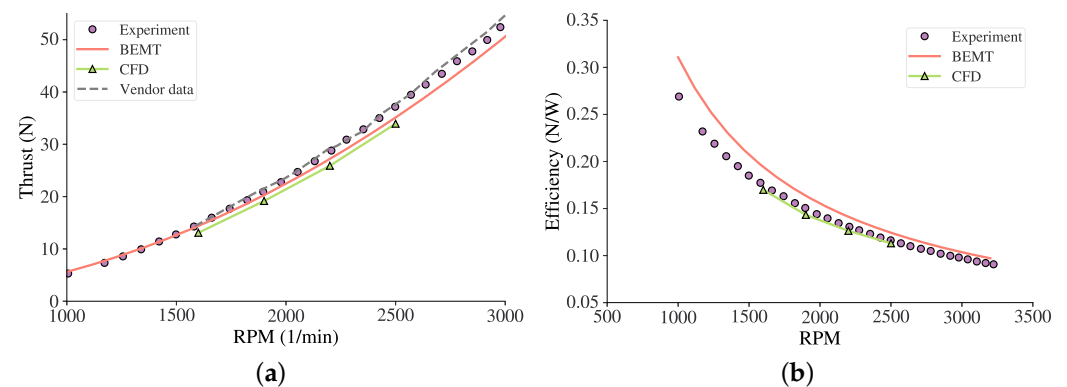

Figure 9. Comparison between experiments, BEMT simulations and CFD simulations for a single rotor. (**a**) Thrust. (**b**) Efficiency.

Further details of the flow pattern are given in Figure 10, which shows the averaged velocity magnitude from the CFD simulations in a vertical slice at the four simulated angular speeds. The flow pattern is the same for all angular speeds, but with an increase in the velocity magnitude for higher angular speeds. Flow is accelerated from the static air above the rotor, resulting in a high-velocity wake below the rotor. There is a low-velocity region just underneath the rotor hub where there is no pitched airfoil to accelerate the flow. The wake clearly contracts into a vena contracta, with a close-to-uniform velocity in the center of the blade and a sharp fall-off to zero at the sides. Although the wakes become closer towards the center at a distance from the rotor, a lower-velocity core remains at the center.

Figure 11 shows the vertical velocity component as a function of radial distance, at a distance of 0.115 m below the rotor. This is the distance where the lower rotor is placed for the coaxial simulations. The predicted inflow velocity from the coaxial BEMT model is shown as dashed lines. There appears to be good agreement between the velocity simulated from CFD and the velocity predicted from the BEMT model. This indicates that the BEMT model is also applicable to coaxial systems.
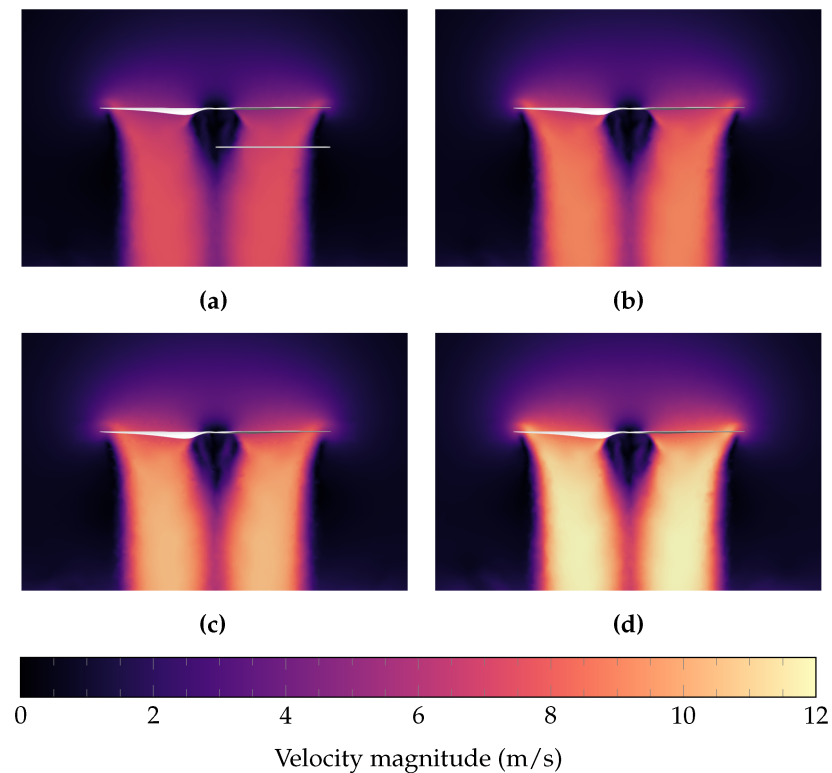
Figure 10. Magnitude of velocity vector for single-rotor setup at varying RPM. The grey line indicated in (**a**) shows the position of the second rotor for the coaxial setup. (**a**) RPM = 1600. (**b**) RPM = 1900. (**c**) RPM = 2200. (**d**) RPM = 2500.
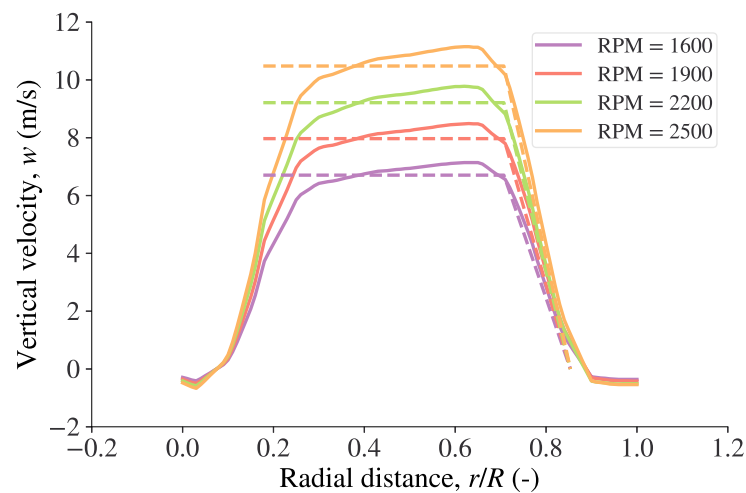

Figure 11. Vertical velocity at a vertical distance 0.115 m from the rotor (indicated by the grey line in Figure 10), estimating inflow velocity for the lower rotor in the coaxial setup. The dashed lines are the values predicted from the coaxial BEMT model.

5.3. Coaxial Rotor Validation

The same validation was performed for a coaxial setup, using two T-MOTOR G28x9.2 rotors. The rotors are placed at a distance of 0.115 m apart, rotating in opposite directions at the same angular velocity. Figure 12a shows a comparison of the computed thrust with BEMT and CFD against the experimental values for varying angular velocities. The experimental results and CFD results for the upper rotor are almost identical to the isolated rotor results, indicating that the upper rotor is not significantly affected by the lower

rotor. Note that for the CFD results, the thrust values presented here are averaged results. In the coaxial setup, the thrust will oscillate based on the angular position of the rotor relative to the lower rotor. The lower rotor, as expected, shows lower thrust than the upper rotor. For the experiments, the thrust values are 60% to 65% of the upper rotor. The CFD results are again close to the experimental results. For the lower rotor there is a maximum of 6.5% discrepancy in the results. The coaxial BEMT model gives an underprediction of the thrust from 10% at lower angular speeds to 20% at higher angular speeds.
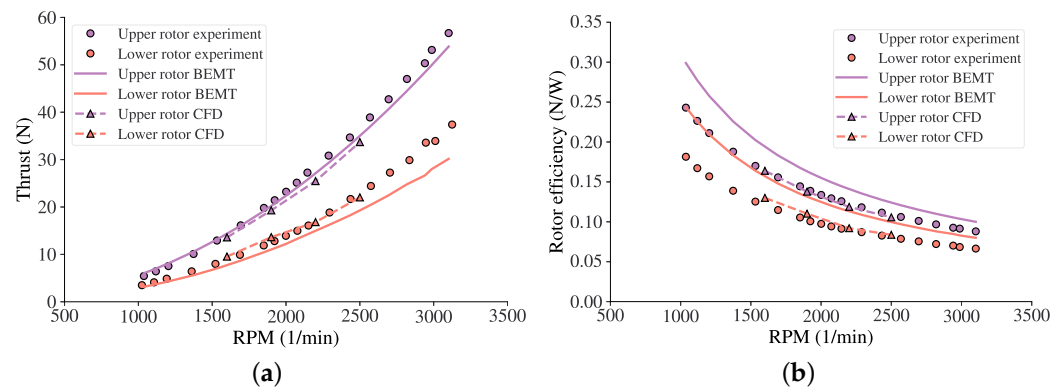

Figure 12. Comparison between experiments, BEMT simulations and CFD simulations for the coaxial rotor setup. (**a**) Thrust. (**b**) Efficiency.

Figure 12b shows a comparison of the computed efficiency with BEMT and CFD against the experimental values for varying angular velocities. The efficiency for the CFD simulations again follow the trend of the experiments and have values in good agreement with the experimental values. The BEMT method also follows the same trends, but significantly overpredicts the efficiency for the lower rotor with values 20% to 35% higher than the experimental values. This is an indication that there are interactions between the rotors not captured by the simple coaxial model used in this work. Still, as both the CFD method and the BEMT method predict the same trends as the experiments, both in terms of thrust and efficiency, they should provide valuable insight on the effect of changing the pitch of the lower rotor.

The CFD method has the additional benefit of capturing more flow details and rotor interactions than the BEMT method. Figure 13 shows the averaged velocity magnitude from the CFD simulations in a vertical slice at the four simulated angular speeds. The velocities are larger than in the corresponding Figure 10 for the single-rotor setup, due to the additional thrust from the lower rotor. It is also clear that the outer region of the lower rotor operates outside the wake of the upper rotor. The total wake from both rotors is also wider than for the single rotor, with a higher velocity core from the combined wake of the two rotors and a lower velocity outer rim from the wake generated by the outer region of the lower rotor. These observations are similar to previous simulations performed on a larger coaxial rotor system by Jinghui et al. [14].
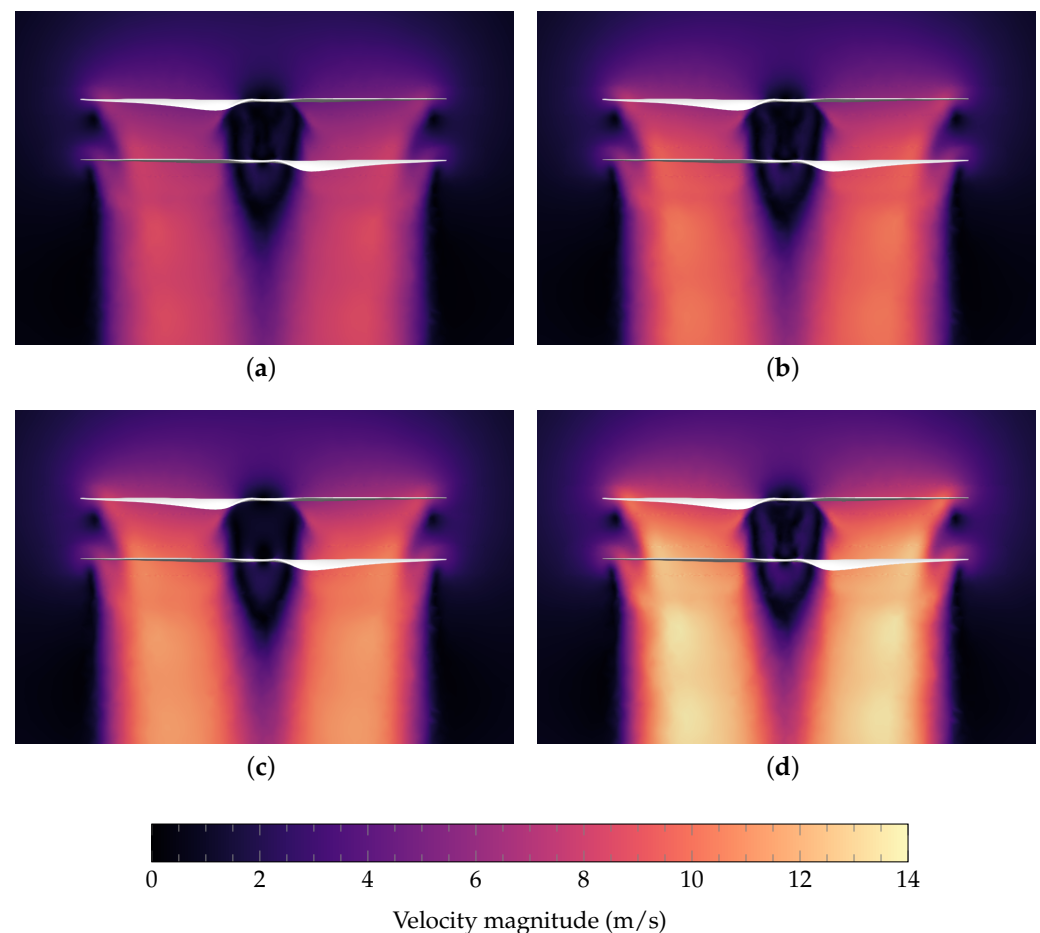
Figure 13. Magnitude of velocity vector for coaxial rotor setup at varying RPM. (**a**) RPM = 1600. (**b**) RPM = 1900. (**c**) RPM = 2200. (**d**) RPM = 2500.

6. Results

In this section, the impact of the lower rotor pitch on efficiency is investigated. First, the BEMT method is used to sweep over a range of pitches for the lower rotor. The case of RPM = 2200 and a pitch of $9.2''$ for both rotors is used as a reference case. The pitch of the lower rotor is varied from $8.2''$ to $16.2''$ and the RPM of the lower rotor is adjusted to give the same total thrust for each case. Using the CFD method, three pitches of $12.2''$, $13.2''$ and $14.2''$ are simulated, while also adjusting the RPM of the lower rotor until the same total thrust as the reference case is obtained.

The resulting efficiencies are plotted in Figure 14. The BEMT results indicate a clear peak in efficiency at a pitch of $14''$, with an improvement in efficiency of 2.3%. For the CFD method, the peak is found at a pitch of $13.2''$, and with a higher improvement in efficiency of 5.0%. Both methods predict a peak in the efficiency, and the location of the peak is also found at a similar pitch, but the CFD method predicts a higher efficiency value. To compare the two solutions, Figure 15 shows the thrust along the rotor for the two methods for a pitch of $14.2''$. For the middle part of the rotor, the methods have similar thrust, which indicates that the coaxial model in the BEMT method works well. The transition from the part of the rotor that is inside the slipstream to the outer part of the rotor is sharper in the BEMT solution than in the CFD solution. Although the coaxial model has a linear transition in incoming velocity, as seen in Figure 11, there should be an additional smoothing to match the CFD solution. Additionally, the tip correction appears to be too high, as the thrust tapers off towards the tip of the rotor faster than in the CFD solution. Despite these differences, the BEMT method captures the overall behavior of the lower rotor.
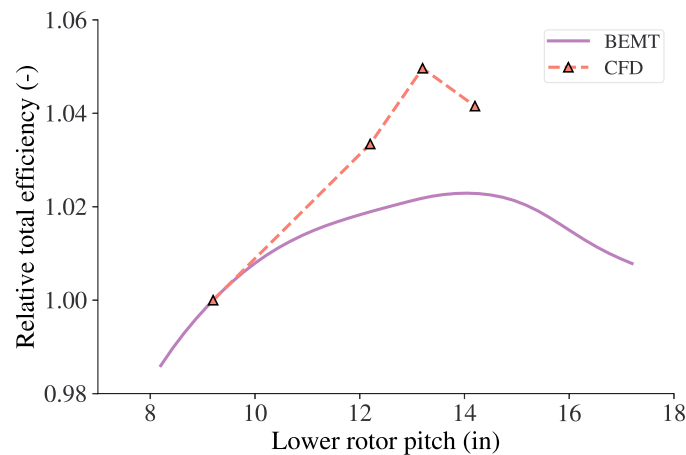
Figure 14. Total efficiency relative to total efficiency at pitch 9.2″ for the coaxial rotor system as a function of lower rotor pitch.
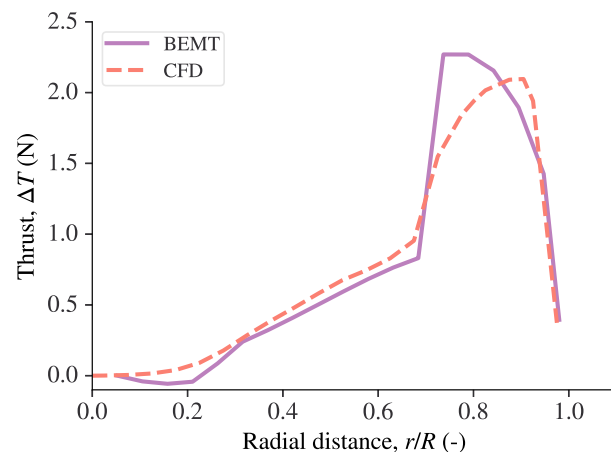

Figure 15. Comparison of BETM and CFD for thrust along blade for pitch 14.2″.

Figure 16a shows the thrust along the blade from the BEMT method for three different pitches. It is clear that the majority of the thrust is produced at the outer region, outside of the wake from the upper rotor. As the pitch is increased from 9.2″ to 14.2″, the amount of thrust generated from the inner region is increased while the amount of thrust from the outer region is decreased. The reduction in thrust from the outer region is due to the reduction in angular velocity to maintain the same total thrust. The angular velocity is reduced from RPM = 2200 to RPM = 1714 for the lower rotor. This also leads to an overall improvement in aerodynamic efficiency, as shown in Figure 16b. This means that at the original angular velocity of RPM = 2200 and at the original pitch of 9.2″, the airfoil is not operating at its optimal point. Increasing the pitch to 14.2″ brings it close to the peak efficiency in the outer region, as evident in Figure 16b. When the pitch is further increased to 17.2″, the airfoil is still below its stall point, hence lift is still increased and the angular velocity is further reduced to RPM = 1554 to maintain the same total thrust. However, at this pitch, the outer region has an angle of attack higher than the optimal point, thus drastically reducing the aerodynamic efficiency by almost half compared to a pitch of 14.2″. Hence, even though the efficiency is improved for the inner region, the total efficiency is still reduced.
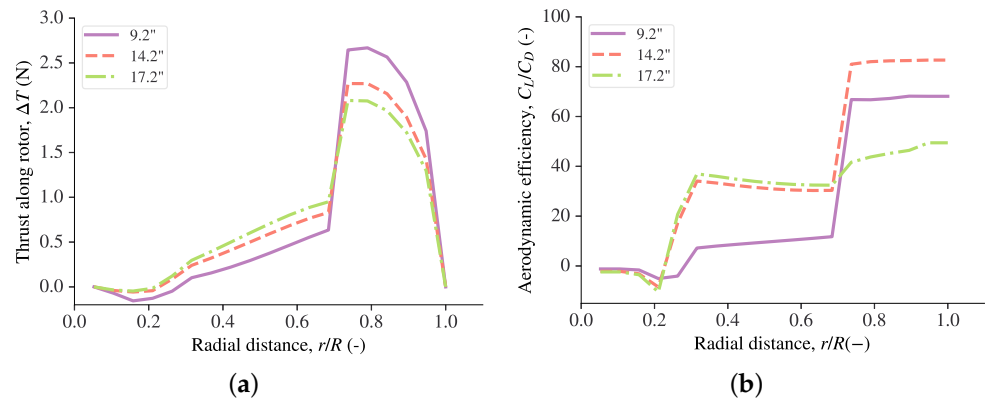
Figure 16. BEMT results along the blade for the lower rotor for three different pitches. (**a**) Thrust along blade. (**b**) Aerodynamic efficiency along blade.

Next, some results from the corresponding CFD simulations are shown, to give further details of the influence of changing the lower rotor pitch. Figure 17b shows contour plots of the pressure coefficient at a radial distance of $r = 0.3R$, i.e., in the inner region of the blade. The plot also shows the flow pattern as seen by the blade (the velocity subtracted by the angular velocity), visualized using the line integral convolution technique [45]. For the pitch of 9.2″, the incoming flow comes in at a negative angle of attack, leading to a region of low pressure near the leading edge at the beginning of the pressure side of the airfoil. At the pitch of 14.2″, the incoming flow operates at an angle of attack close to zero, hence leading to a pressure profile that is more optimal, with lower pressure on the suction side and higher pressure on the pressure side compared to the original pitch.
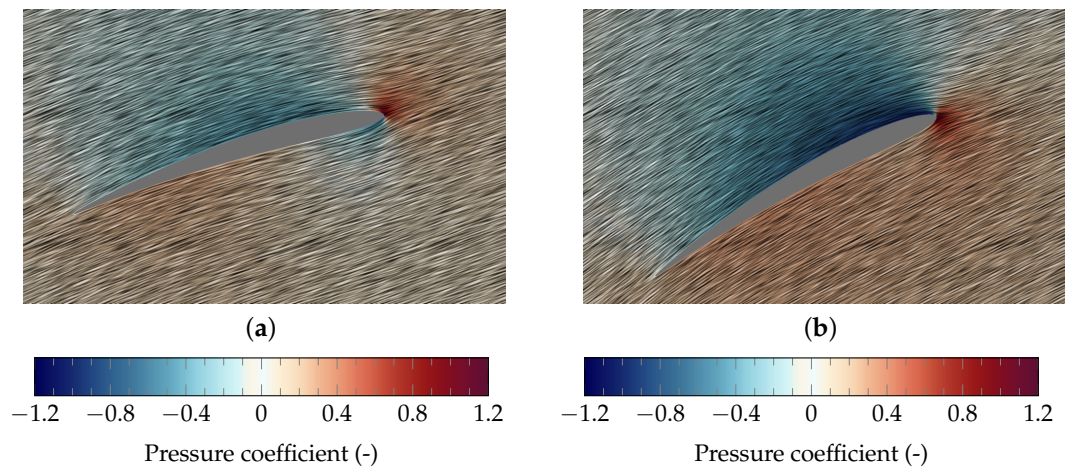

Figure 17. Pressure coefficient and flow pattern (as seen from the rotor) for the lower rotor at radius $r = 0.3R$ for two different pitches. (**a**) Pitch 9.2″. (**b**) Pitch 14.2″.

The pressure coefficient over the blade for the two cases is also plotted in Figure 18. Here, the drop in pressure at the leading edge for pitch 9.2″ is clearly seen. It is also apparent that for pitch 14.2″, the pressure is lower on the suction side and higher on the pressure side over the entirety of the airfoil compared to the original pitch of 9.2″.
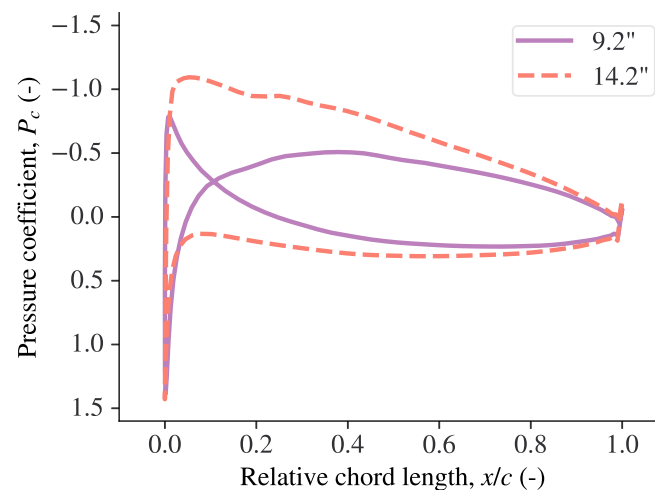
Figure 18. Pressure coefficient over the lower rotor blade at radius $r = 0.3R$ for two different pitches.

7. Conclusions

A computational study was performed investigating the influence of varying pitch on the rotor efficiency in a coaxial rotor setup. An efficient blade element momentum theory method for a coaxial rotor system was developed, and detailed computational fluid dynamics simulations were performed. The chosen rotor has a diameter of 71.12 cm, corresponding to a typical rotor size used in medium-sized multirotor drones.

The two methodologies were validated by comparing against experiments on a single-rotor system and a coaxial rotor system. The CFD methodology showed good agreement on both systems. The BEMT methodology reproduced the experimental trends, but over-predicted the efficiency of the coaxial rotor system.

The results showed that an optimum value for the pitch of the lower rotor could be obtained with both methods, where the total efficiency of the coaxial system was increased by 2% to 5% compared to using the same pitch for the upper and lower rotors. This was found to be due to increasing the efficiency of both the inner region of the rotor, acting in the wake of the upper rotor, and the outer region of the rotor.

Future work will focus on further optimizing the rotor setup. As the current work only used a single pitch for the entire rotor, further increases in the efficiency could be obtained by tailoring the rotor pitch fully to a coaxial setup with pitches designed to be optimal over the entire rotor. This could also include using different airfoils for different parts of the rotor to better match the induced angles of attack. Currently, commercial rotor designs are not available for the high pitches proposed in this work. Future work will also aim to manufacture optimized rotor designs to test experimentally. The current work also only considered the situation of a hovering rotor, and having a system in forward flight should also be investigated. Finally, a more detailed study of the rotor dynamics and wake interactions should be performed, as well as investigating full drone setups with rotor–body interactions.

Vetle Byremo Ingebretsen, Sondre Andersen Gysland, Kjell Vistnes Randeberg, Adrian Otter Falch Günther and Abuzar Ghaffari. We also thank the anonymous reviewers for their constructive comments, which helped improve the manuscript.

Conflicts of Interest: The authors declare no conflicts of interest.

References

1. Hassanalian, M.; Abdelkefi, A. Classifications, applications, and design challenges of drones: A review. *Prog. Aerosp. Sci.* **2017**, *91*, 99–131. [CrossRef]
2. Miiller, H.; Palossi, D.; Mach, S.; Conti, F.; Benini, L. F'unfiiber-Drone: A Modular Open-Platform 18-grams Autonomous Nano-Drone. In Proceedings of the Design, Automation & Test in Europe Conference & Exhibition, Virtual, 1–5 February 2021; pp. 1610–1615.
3. Giernacki, W.; Skwierczyński, M.; Witwicki, W.; Wroński, P.; Kozierski, P. Crazyflie 2.0 quadrotor as a platform for research and education in robotics and control engineering. In Proceedings of the 22nd International Conference on Methods and Models in Automation and Robotics (MMAR), Miedzyzdroje, Poland, 28–31 August 2017; pp. 37–42.
4. Shamiyeh, M.; Rothfeld, R.; Hornung, M. A performance benchmark of recent personal air vehicle concepts for urban air mobility. In Proceedings of the 31st Congress of the International Council of the Aeronautical Sciences, Belo Horizonte, Brazil, 9–14 September 2018; Volume 14.
5. Moore, M.D. *Personal Air Vehicle Exploration (PAVE)*; NASA Langley Research Center: Hampton, VI, USA, 2002; pp. 1–48.
6. Bradley, T.H.; Moffitt, B.A.; Fuller, T.F.; Mavris, D.N.; Parekh, D.E. Comparison of design methods for fuel-cell-powered unmanned aerial vehicles. *J. Aircraft* **2009**, *46*, 1945–1956. [CrossRef]
7. Apeland, J. Use of Fuel Cells to Extend Multirotor Drone Endurance. Ph.D. Thesis, University of Stavanger, Stavanger, Norway, 2021.
8. Prior, S.D. Reviewing and investigating the use of Co-Axial rotor systems in small UAVs. *Int. J. Micro Air Veh.* **2010**, *2*, 1–16. [CrossRef]
9. Lei, Y.; Ji, Y.; Wang, C. Optimization of aerodynamic performance for co-axial rotors with different rotor spacings. *Int. J. Micro Air Veh.* **2018**, *10*, 362–369. [CrossRef]
10. Brazinskas, M.; Prior, S.D.; Scanlan, J.P. An empirical study of overlapping rotor interference for a small unmanned aircraft propulsion system. *Aerospace* **2016**, *3*, 32. [CrossRef]
11. Weishäupl, A.B.; Prior, S.D. Influence of Propeller Overlap on Large-Scale Tandem UAV Performance. *Unmanned Sys.* **2019**, *7*, 245–260. [CrossRef]
12. Prior, S.D. *Optimizing Small Multi-Rotor Unmanned Aircraft: A Practical Design Guide*; CRC Press: Boca Raton, FL, USA, 2018.
13. Yoon, S.; Chan, W.M.; Pulliam, T.H. Computations of torque-balanced coaxial rotor flows. In Proceedings of the 55th AIAA Aerospace Sciences Meeting, Grapevine, TX, USA, 9–13 January 2017; p. 52.
14. Jinghui, D.; Feng, F.; Huang, S.; Yongfeng, L. Aerodynamic characteristics of rigid coaxial rotor by wind tunnel test and numerical calculation. *Chin. J. Aeronaut.* **2019**, *32*, 568–576.
15. Kim, Y.T.; Park, C.H.; Kim, H.Y. Three-Dimensional CFD Investigation of Performance and Interference Effect of Coaxial Propellers. In Proceedings of the IEEE 10th International Conference on Mechanical and Aerospace Engineering (ICMAE), Brussels, Belgium, 22–25 July 2019; pp. 376–383.
16. Leishman, J.G.; Ananthan, S. An optimum coaxial rotor system for axial flight. *J. Am. Helicopter Soc.* **2008**, *53*, 366–381. [CrossRef]
17. Leishman, G.J. *Principles of Helicopter Aerodynamics*; Cambridge University Press: Cambridge, UK, 2006.
18. Manwell, J.F.; McCowan, J.; Rogers, A.L. Wind energy explained: Theory, design and application. *Wind Eng.* **2006**, *30*, 169.
19. Schmitz, S. *Aerodynamics of Wind Turbines: A Physical Basis for Analysis and Design*; John Wiley & Sons: Hoboken, NJ, USA, 2020.
20. Glauert, H. Airplane propellers. In *Aerodynamic Theory*; Springer: Berlin/Heidelberg, Germany, 1935; pp. 169–360.
21. Giljarhus, K.E.T. pyBEMT: An implementation of the Blade Element Momentum Theory in Python. *J. Open Source Softw.* **2020**, *5*, 2480. [CrossRef]
22. Virtanen, P.; Gommers, R.; Oliphant, T.E.; Haberland, M.; Reddy, T.; Cournapeau, D.; Burovski, E.; Peterson, P.; Weckesser, W.; Bright, J.; et al. SciPy 1.0: Fundamental Algorithms for Scientific Computing in Python. *Nat. Methods* **2020**, *17*, 261–272. [CrossRef] [PubMed]
23. Leishman, J.G.; Syal, M. Figure of merit definition for coaxial rotors. *J. Am. Helicopter Soc.* **2008**, *53*, 290–300. [CrossRef]
24. Lee, S.; Dassonville, M. Iterative Blade Element Momentum Theory for Predicting Coaxial Rotor Performance in Hover. *J. Am. Helicopter Soc.* **2020**, *65*, 1–12. [CrossRef]
25. Lakshminarayan, V.K.; Baeder, J.D. Computational investigation of microscale coaxial-rotor aerodynamics in hover. *J. Aircr.* **2010**, *47*, 940–955. [CrossRef]
26. Yoon, S.; Chaderjian, N.; Pulliam, T.H.; Holst, T. Effect of turbulence modeling on hovering rotor flows. In Proceedings of the 45th AIAA Fluid Dynamics Conference, Dallas, TX, USA, 22–26 June 2015; p. 2766.
27. Lopez, O.D.; Escobar, J.A.; Pérez, A.M. Computational study of the wake of a quadcopter propeller in hover. In Proceedings of the 23rd AIAA Computational Fluid Dynamics Conference, Denver, CO, USA, 5–9 June 2017; p. 3961.

28. Loureiro, E.V.; Oliveira, N.L.; Hallak, P.H.; de Souza Bastos, F.; Rocha, L.M.; Delmonte, R.G.P.; de Castro Lemonge, A.C. Evaluation of low fidelity and CFD methods for the aerodynamic performance of a small propeller. *Aerosp. Sci. Tech.* **2021**, *108*, 106402. [CrossRef]

29. Barbely, N.L.; Komerath, N.M.; Novak, L.A. A Study of Coaxial Rotor Performance and Flow Field Characteristics. In Proceedings of the 2016 AHS Technical Meeting on Aeromechanics Design for Vertical Lift, San Francisco, CA, USA, 20–22 January 2016.

30. Cornelius, J.K.; Schmitz, S.; Kinzel, M.P. Efficient computational fluid dynamics approach for coaxial rotor simulations in hover. *J. Aircraft* **2020**, *58*, 197–203. [CrossRef]

31. Panjwani, B.; Quinsard, C.; Przemysław, D.G.; Furseth, J. Virtual Modelling and Testing of the Single and Contra-Rotating Co-Axial Propeller. *Drones* **2020**, *4*, 42. [CrossRef]

32. Menter, F.R. Two-equation eddy-viscosity turbulence models for engineering applications. *AIAA J.* **1994**, *32*, 1598–1605. [CrossRef]

33. Weller, H.G.; Tabor, G.; Jasak, H.; Fureby, C. A tensorial approach to computational continuum mechanics using object-oriented techniques. *Comput. Phys.* **1998**, *12*, 620–631. [CrossRef]

34. Jasak, H.; Jemcov, A.; Tukovic, Z. *OpenFOAM: A C++ Library for Complex Physics Simulations*; CMND. IUC: Dubrovnik, Croatia, 2007; Volume 1000.

35. Farrell, P.; Maddison, J. Conservative interpolation between volume meshes by local Galerkin projection. *Comput. Method Appl. Mech. Eng.* **2011**, *200*, 89–100. [CrossRef]

36. Nordic Unmanned. Staaker BG-200. Available online: https://nordicunmanned.com/drones/staaker-bg200/ (accessed on 10 March 2022).

37. PRODRONE. PD6B-Type2. Available online: https://www.prodrone.com/products/pd6b-type2/ (accessed on 10 March 2022).

38. Czerhoniak, M.S. Scaling up the Propulsion System of an Aerial and Submersible Multirotor Vehicle. Ph.D. Thesis, Rutgers University-School of Graduate Studies, Piscataway, NJ, USA, 2018.

39. Selig, M.S. *Summary of Low Speed Airfoil Data*; SOARTECH Publications: Virginia Beach, VI, USA, 1995.

40. Selig, M.S. UIUC Airfoil Data Site. 1996. Available online: https://m-selig.ae.illinois.edu/ads.html (accessed on 10 March 2022).

41. Drela, M. XFOIL: An analysis and design system for low reynolds number airfoils. In *Low Reynolds number Aerodynamics*; Springer: Berlin/Heidelberg, Germany, 1989; pp. 1–12.

42. Marten, D.; Wendler, J.; Pechlivanoglou, G.; Nayeri, C.N.; Paschereit, C.O. QBLADE: an open source tool for design and simulation of horizontal and vertical axis wind turbines. *Int. J. Emer. Tech. Adv. Eng.* **2013**, *3*, 264–269.

43. Cadence Design Systems. Pointwise® V18.4R4. Available online: https://www.pointwise.com (accessed on 25 December 2021).

44. T-MOTOR. T-MOTOR U8II. Available online: https://store.tmotor.com/goods.php?id=476 (accessed on 8 Febraury 2019).

45. Cabral, B.; Leedom, L.C. Imaging vector fields using line integral convolution. In Proceedings of the 20th annual conference on Computer graphics and interactive techniques, Anaheim, CA, USA, 2–6 August 1993; pp. 263–270.